SANDIA REPORT

SAND2005-51745174
Unlimited Release
Printed September 2005

An Example Uncertainty and Sensitivity Analysis for Reactive Transport at the Horonobe Site for Performance Assessment Calculations

Scott C. James and Alex Cohan

Prepared by
Sandia National Laboratories
Albuquerque, New Mexico 87185 and Livermore, California 94550

Sandia is a multiprogram laboratory operated by Sandia Corporation,
a Lockheed Martin Company, for the United States Department of Energy's
National Nuclear Security Administration under Contract DE-AC04-94AL85000.

Approved for public release; further dissemination unlimited.

Issued by Sandia National Laboratories, operated for the United States Department of Energy by Sandia Corporation.

NOTICE: This report was prepared as an account of work sponsored by an agency of the United States Government. Neither the United States Government, nor any agency thereof, nor any of their employees, nor any of their contractors, subcontractors, or their employees, make any warranty, express or implied, or assume any legal liability or responsibility for the accuracy, completeness, or usefulness of any information, apparatus, product, or process disclosed, or represent that its use would not infringe privately owned rights. Reference herein to any specific commercial product, process, or service by trade name, trademark, manufacturer, or otherwise, does not necessarily constitute or imply its endorsement, recommendation, or favoring by the United States Government, any agency thereof, or any of their contractors or subcontractors. The views and opinions expressed herein do not necessarily state or reflect those of the United States Government, any agency thereof, or any of their contractors.

Printed in the United States of America. This report has been reproduced directly from the best available copy.

Available to DOE and DOE contractors from
U.S. Department of Energy
Office of Scientific and Technical Information
P.O. Box 62
Oak Ridge, TN 37831

Telephone: (865) 576-8401
Facsimile: (865) 576-5728
E-Mail: reports@adonis.osti.gov
Online order: http://www.doe.gov/bridge

Available to the public from
U.S. Department of Commerce
National Technical Information Service
5285 Port Royal Rd
Springfield, VA 22161

Telephone: (800) 553-6847
Facsimile: (703) 605-6900
E-Mail: orders@ntis.fedworld.gov
Online order: http://www.ntis.gov/help/ordermethods.asp?loc=7-4-0#online

SAND2005-51745174
Unlimited Release
Printed September 2005

An Example Uncertainty and Sensitivity Analysis Including Reactive Transport at the Horonobe Site for Performance Assessment Calculations

Scott C. James
Sandia National Laboratories
Geohydrology Department
P.O. Box 5800
Albuquerque, New Mexico 87185-0735
scjames@sandia.gov

Alex Cohan
Sandia National Laboratories
Geohydrology Department
P.O. Box 5800
Albuquerque, New Mexico 87185-0735
acohan@sandia.gov

Abstract

Given pre-existing Groundwater Modeling System (GMS) models of the Horonobe Underground Research Laboratory (URL) at both the regional and site scales, this work performs an example uncertainty analysis for performance assessment (PA) applications. After a general overview of uncertainty and sensitivity analysis techniques, the existing GMS site-scale model is converted to a PA model of the steady-state conditions expected after URL closure. This is done to examine the impact of uncertainty in site-specific data in conjunction with conceptual model uncertainty regarding the location of the Oomagari Fault. A heterogeneous stochastic model is developed and corresponding flow fields and particle tracks are calculated. In addition, a quantitative analysis of the ratio of dispersive to advective forces, the F-ratio, is performed for stochastic realizations of each conceptual model. Finally, a one-dimensional transport abstraction is modeled based on the particle path lengths and the materials through which each particle passes to yield breakthrough curves at the model boundary. All analyses indicate that accurate characterization of the Oomagari Fault with respect to both location and hydraulic conductivity is critical to PA calculations. This work defines and outlines typical uncertainty and sensitivity analysis procedures and demonstrates them with example PA calculations relevant to the Horonobe URL.

Acknowledgement: This project was funded by Japan Nuclear Cycle Development Institute (JNC). This work was conducted jointly between Sandia National Laboratories (SNL) and JNC under a joint JNC/U.S. Department of Energy (DOE) work agreement. Performance assessment calculations were conducted and analyzed at SNL based on a preliminary model by Kashima, Quintessa, and JNC and include significant input from JNC to make sure the results are relevant for the Japanese nuclear waste program.

Table of Contents

List of Figures

List of Tables

1. Introduction

Characterization of uncertainty associated with flow and transport models is critical to environmental models used for performance and risk assessment. A systematic uncertainty analysis provides insight into the level of confidence in model results and aids in assessing how various model estimates should be weighed. Uncertainty analyses use available information to quantify the degree of confidence in existing data and models. Further, they can identify the key sources of uncertainty (such as data gaps) that merit additional site characterization as well as the sources of uncertainty that are not important for performance assessment (PA). However, uncertainty analyses do not reduce uncertainty – that can only come with the collection of additional data. Instead, the goal is to understand judgments associated with modeling despite applicability of a model being inherently limited by uncertainties in data. A quantitative uncertainty analysis can ascertain the robustness of model conclusions particularly when data are limited and when simplifying assumptions have been used. Ultimately, models should help target data gathering efforts. In addition, alternate conceptual models can play a large role in process analysis. All valid conceptual models of a site should be included in an uncertainty and sensitivity analysis because they may yield different results and insight into the various processes modeled. A detailed introduction to uncertainty and sensitivity analyses may be found in the work of James (2004).

In this work, an existing model provided by Quintessa for the dewatering of the Horonobe Underground Research Laboratory (URL) is modified to make it amenable to an example PA model. Actual site data from six exploratory boreholes are incorporated into its design and stochastic particle tracking realizations are presented. In addition, a synthetic parameter measuring the ratio of diffusive to advective forces, the F-ratio, is calculated along the particle tracks and analyzed. Finally, a one-dimensional advection-dispersion-reaction model is implemented along the particle tracks to generate breakthrough curves. This work may be used as an example for future, more detailed PA models.

2. Model Background

2.1 Background

Environmental systems are inherently unpredictable due to our inability to accurately represent conditions and parameters across space and time. For this reason, environmental systems are generally represented as stochastic processes. James (2004) presents a general definition of variability and defines how parameters can be represented with random values because of natural uncertainty.

Uncertainties in model parameter estimates stem from a variety of sources. While in principle, many parameters could be measurable up to any desired precision, often there are significant uncertainties associated with field and laboratory measurements. Some uncertainties arise from measurement errors, which involve: 1) random errors in analytic devices (e.g., the imprecision of monitors that measure temperature); 2) systematic biases due to imprecise calibration; or, 3) inaccuracies in the assumptions used to infer the actual quantity of interest from the readings of a ‘surrogate’ variable (e.g., inferring K through water level measurements). Other potential sources of uncertainties in estimates of parameters include misclassification, estimation of parameters through a small sample, and estimation of parameters through non-representative samples. Ultimately, uncertainty in model application arises from uncertainties associated with

measurement data used for the model evaluation. When reviewing this PA example, the reader should look for other areas where model uncertainty could be investigated and consider examining these areas with additional modeling activities.

2.2 Horonobe Site Data

Six exploratory boreholes, HDB-1, -3, -4, -5, -6, and -8, were drilled within the domain of the site-scale model. Data collected from these boreholes include among others: fracture frequency, bulk density, temperature, porosity, and saturation. Fracture frequency is chosen as the parameter of interest for this study because of the large and detailed data set available. Stochastic realizations of the model domain are constrained by fracture frequency distributions in each borehole. This parameter was selected because of the extensive data set available and because these data fit into the Groundwater Modeling System (EMRL, 2003) (GMS) framework well. GMS allows for definition of multiple distinct material types in a model. Corresponding to last year's model (James, 2004), five material types are used in this modeling effort although the newest version of GMS no longer limits the number of material types. Observed fracture frequency ranges from 0 to 20 fractures/m: borehole data with no fractures/m are defined as Material 1; 1–5 fractures/m as Material 2; 6–10 as Material 3; 11–15 as Material 4; and, 16–20 as Material 5 as shown in Figure 1. Because hydraulic conductivity is assumed to be related to fracture frequency (i.e., more highly fractured portions of the media are more conductive), each material is assigned a hydraulic conductivity multiplier, $K_{material}$, which is a parameter used to modify the original hydraulic conductivity to derive a heterogeneous field (see derivation below and Table 1).

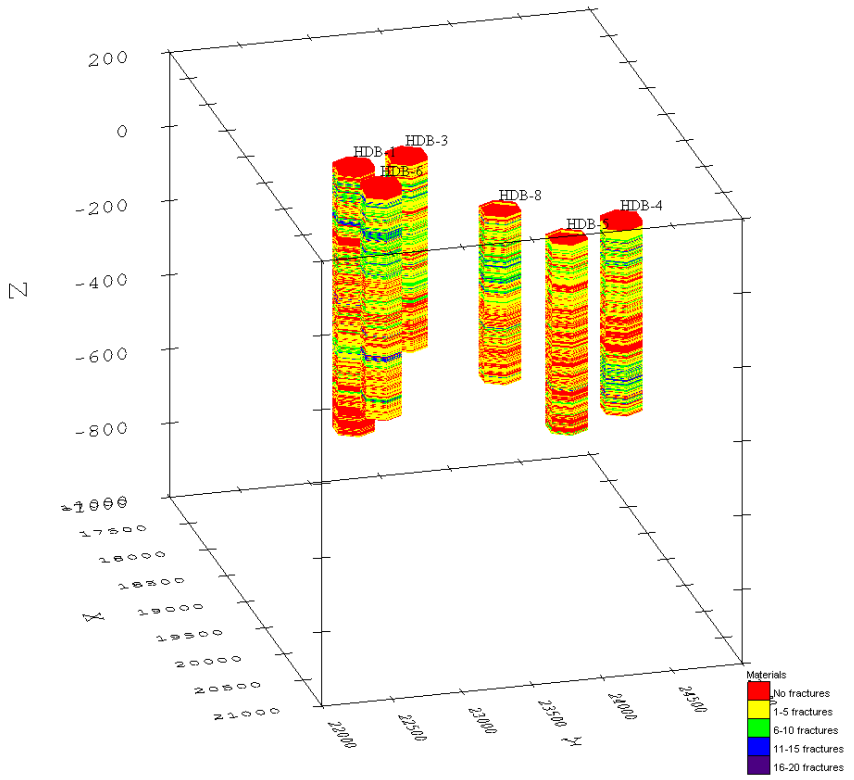

Figure 1: Boreholes HDB-1, -3, -4, -5, -6 and -8 are shown with color indicating the material type based on fracture frequency.

2.3 The Quintessa GMS Model of Horonobe

A detailed description of the uncertainties present in a typical modeling effort may be found in the work of James (2004). Quintessa developed a GMS model of the Horonobe URL site, which began with a regional-scale model where the average surface elevation was interpolated from a detailed topographic map. The model covers 49 km (north-south) by 37.5 km (east-west) and is 5 km deep with a 100-column×100-row×80-layer grid (800,000 cells) using natural boundary conditions (e.g., the seacoast) when possible. The geologic properties of this model (e.g., hydraulic conductivity) are based on the known geology of the area. Within the regional-scale model domain, Quintessa developed both steady state and transient site-scale GMS models of the Horonobe site to study the effects of dewatering during URL construction. This site-scale model is 4.02 km (north-south) by 3 km (east-west) by 1,250 m deep and is discretized to an 83-column×72-row×124-layer grid (741,024 cells) with local refinement in the URL region and near the water table as shown in Figure 2. No recharge is applied to either the regional- or site-scale models. The boundary conditions for the site-scale model were established through interpolation of the results (because of mesh inconsistencies) from the regional-scale model.

The Quintessa GMS model investigated several conceptual models of the Oomagari Fault that traverses the Horonobe site-scale model domain. The Oomagari Fault is distinct from the remaining fractured media in that it comprises a fairly wide zone of altered geologic material due to long-term seismic activity. Because site characterization at Horonobe is just beginning, the exact location of the fault as well as its hydraulic conductivity (low or high) is unknown. Using Quintessa's steady-state site-scale model, Sandia National Laboratories has developed a stochastic model based on site data to demonstrate the processes and procedures typical of PA and decision analysis models.

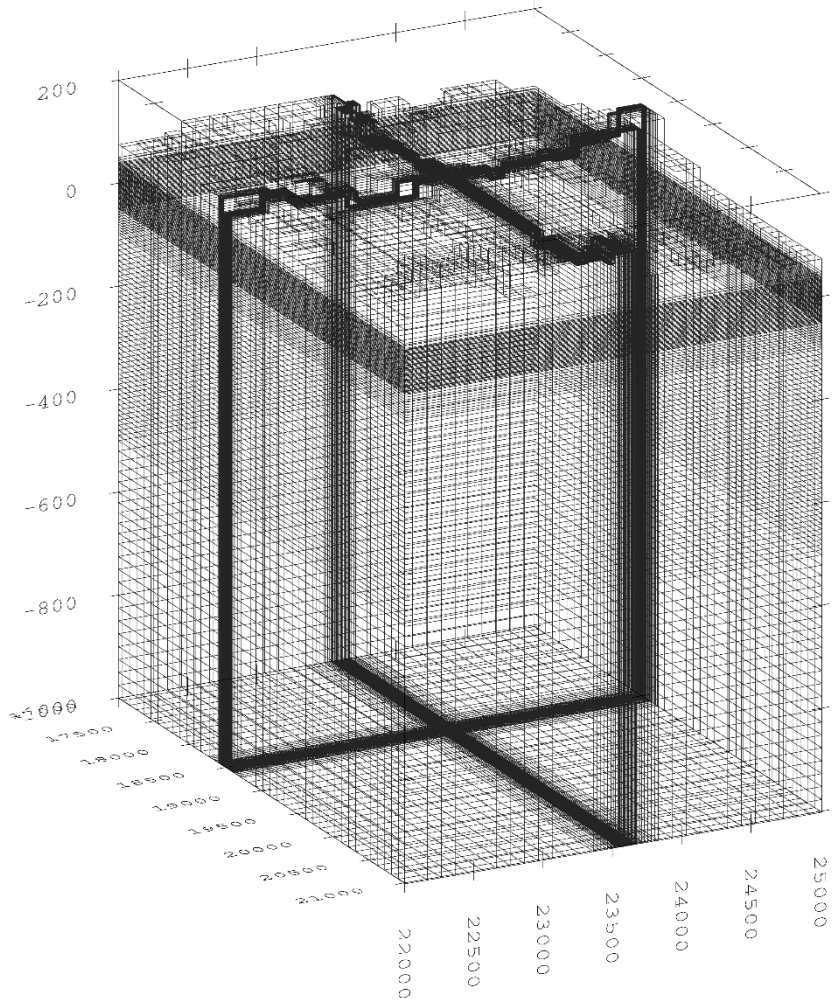

Figure 2: Finite difference mesh used in the Quintessa site-scale model of the Horonobe URL. The figure is stretched by a factor of 3.5 in the vertical to more clearly illustrate the mesh. Axes coordinates are given in meters.

Quintessa generated four fundamental conceptual models of the Horonobe URL each with the Oomagari Fault in an alternate position (center or Case C, west or Case W, east or Case E, and no fault or Case NF). As subsets of each conceptual model, the fault, if present, is assigned either high or low hydraulic conductivity with the remaining model domain also assigned either high or low hydraulic conductivity (a total of 15 alternate conceptual models). In this work, stochastic heterogeneous hydraulic conductivity fields based on the borehole data for both high and low hydraulic conductivity faults using each of Quintessa's four fundamental conceptual models were generated. Specifically, each fault location (Cases C, E, and W) with both high and low (H and L) values of hydraulic conductivity for the fault relative to the surrounding medium (where the fault acts as either a conduit or barrier to flow) and one case with no fault were examined (Case NF). All models assume base hydraulic conductivities of $K_i = 10^{-7}$ m/s for the non-fault medium. The first three fundamental conceptual models (low fault hydraulic conductivity, Cases CL, WL, and EL) specify $K_i = 10^{-10}$ m/s for the fault and the second three, CH, WH, and EH specify $K_i = 10^{-5}$ m/s as the base hydraulic conductivity for the fault model cells. For the conceptual model with no fault, the base hydraulic conductivity is

$K_i = 10^{-7}$ m/s everywhere. All original Quintessa hydraulic conductivity fields are modified by stochastic random material fields.

3. Model Development

3.1 Heterogeneous Hydraulic Conductivity Field Generation

The T-PROGS (Carle, 1999) module in GMS is used to generate 50 equally probable heterogeneous material fields conditioned on borehole data based on transition probability statistics (EMRL, 2002). Using the defined material types (i.e., fracture frequency) and their associated depths, T-PROGS calculates the probability of transition between materials (shown in Figure 1) and assigns material properties to each finite difference cell in the model based on the resulting geostatistics.

When generating the heterogeneous hydraulic conductivity field based on the five distinct materials in T-PROGS, it is important to ensure that the volume-weighted geometric mean hydraulic conductivities are equal between the original "homogeneous" Quintessa model and the heterogeneous model developed here. The volume-weighted geometric mean is defined as:

$$GM(K) = \prod_{i=1}^{N} K_i^{\frac{V_i}{V_{\text{total}}}}, \qquad \text{* MERGEFORMAT (1)}$$

where $GM(K)$ is the geometric mean of the model's hydraulic conductivity, K_i is the hydraulic conductivity of the i^{th} Quintessa MODFLOW cell, V_i is the corresponding volume of the cell, and V_{total} is the total volume of the model domain (volume of all N cells).

The goal is to generate a heterogeneous hydraulic conductivity field using the T-PROGS material fields where each successive material has an order of magnitude increment in hydraulic conductivity such that

$$K_{\text{material}} = \alpha K_{f_j}, \qquad \text{* MERGEFORMAT (2)}$$

where

$$K_{f_j} = 10^{j-2}, \qquad \text{* MERGEFORMAT (3)}$$

and j ranges from 1 to 5 for each of the five materials available for cell i. The coefficient α must be selected to ensure that the homogeneous and heterogeneous hydraulic conductivity fields have equal geometric means. The heterogeneous hydraulic conductivity of each MODFLOW cell is defined as

$$K_{\text{heterogeneous}_i} = K_{\text{material}} K_i = \alpha K_{f_j} K_i. \qquad \text{* MERGEFORMAT (4)}$$

Substituting * MERGEFORMAT (4) into the definition of the geometric mean given by * MERGEFORMAT (1), yields

$$GM(K_{\text{heterogeneous}}) = GM(K_{\text{material}} K) = GM(K_{\text{material}}) GM(K). \text{* MERGEFORMAT (5)}$$

For the two sides of the preceding equation to be equal, $GM(K_{\text{material}})$ must be unity. To satisfy this requirement,

$$\alpha = \frac{1}{GM\left(K_{f_j}\right)}. \qquad \text{* MERGEFORMAT (6)}$$

Using the 50 hydraulic conductivity fields generated by T-PROGS yields 50 values for α, which has an average of 1.2459 and a standard deviation of 0.0337. It should be noted that α is independent of the initial hydraulic conductivity field and only a function of the material fields generated by T-PROGS. Table 1 summarizes the material field information.

Table 1: Fracture frequency related to material type and corresponding hydraulic conductivity multiplier. The corresponding proportions of each material from the raw borehole data sets are also presented.

Fracture frequency	Material, j	K_{material}	Proportion
0	1	0.1	30.3%
1–5	2	1.2	53.3%
6–10	3	12.5	13.5%
11–15	4	124.5	2.5%
16–20	5	1,245.9	0.5%

Recall that this is an example PA model and therefore some of the values used in the process are contrived (e.g., K_{material} in Table 1). An actual PA model would require site-specific parameters (i.e., the hydraulic conductivity as a function of fracture frequency) should be measured. Also, it is assumed that the borehole data are sufficiently representative of the entire site when T-PROGS extrapolates these data to the entire model domain. In a formal PA model, this assumption would need to be substantiated.

A total of 50 random material fields were generated with T-PROGS and each was used to create a corresponding random hydraulic conductivity field. GMS was used to solve the resulting flow field subject to the boundary conditions supplied by the regional scale Quintessa model (heads extracted from the regional scale model at the appropriate site scale model boundaries). Table 2 lists the averages (and standard deviations) of the number of grid blocks composed of Materials 1 through 5. Across all 50 material fields from T-PROGS, on average the model is composed of 29.8% Material 1, 53.3% Material 2, 13.8% Material 3, 2.5% Material 4, and 0.5% Material 5, which is consistent with the fracture frequency measurements from the boreholes that are listed in Table 1.

Table 2: Average (and standard deviation) of the number of model cells of each material type.

Material 1	Material 2	Material 3	Material 4	Material 5
220,962 (3,721)	395,287 (2,905)	102,509 (2,185)	18,567 (1003)	3,700 (383)

Once each realization has been completed, the data are exported to an ASCII text file where a FORTRAN pre-processor reads in the material data and original GMS hydraulic conductivity field and then generates a new hydraulic conductivity field based on both inputs. Table 1 defines material properties and their associated hydraulic conductivity multiplier, K_{material}.

Figure 3 shows: (a) the original log hydraulic conductivity field (note the low hydraulic conductivity fault); (b) one realization of the material field generated with T-PROGS; and, (c) the resulting log hydraulic conductivity field equal to the original hydraulic conductivity field with each cell's K value multiplied by $K_{material}$ from the corresponding cell of the material field. The high hydraulic conductivity fault remains, but the overall hydraulic conductivity field for the system is now heterogeneous with geometric mean equal to the hydraulic conductivity of the Quintessa model.

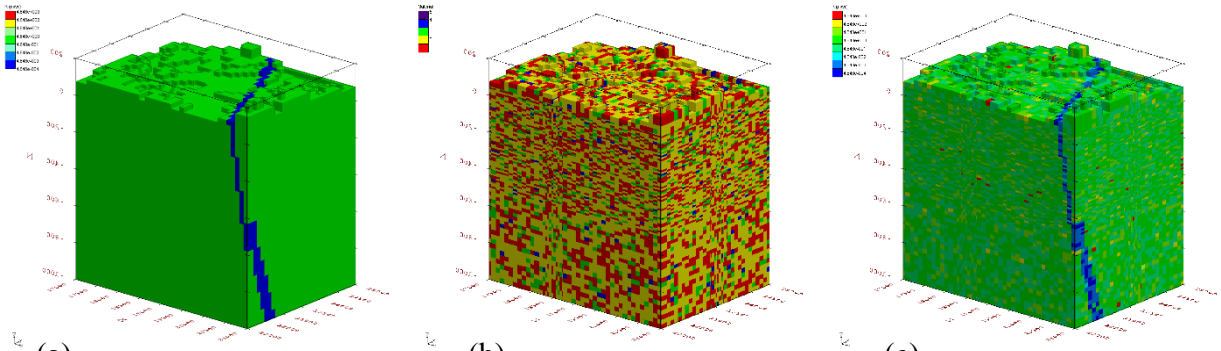

(a) (b) (c)

Figure 3: (a) The original hydraulic conductivity field with low hydraulic conductivity fault; (b) the stochastic material multiplier field; and (c) the resulting hydraulic conductivity field (Case CL).

3.3 Particle Tracking

Particles were released at 500 m depth in each of the boreholes of Figure 1 (a total of six particles) and they were tracked until they exit of the model boundaries. Within a conceptual model, differences in particle path lengths and velocities (travel times) are due to the heterogeneity of the hydraulic conductivity field. Between conceptual models, the placement of the fault and whether it is modeled as a low or high hydraulic conductivity feature also yields variability in particle path lengths and velocities. Descriptive statistics for path lengths and velocities among the 50 stochastic hydraulic conductivity fields for each conceptual model are listed in Table 3. Results are also compared across conceptual models to identify differences due to fault location. Figure 4 illustrates an example of the GMS particle tracking results for the hydraulic conductivity field of Figure 3c (Case CL). The open circles are particle release locations and the filled, red circles are their locations upon crossing the model boundary. The colors on the plots indicate the hydraulic head calculated with GMS where values range from about 50 m (blue) to about 150 m (red). Clearly, particles are, in general, moving downward, but they exit the system through the lateral boundaries because of the no-flow condition at the bottom of the model.

Table 3: Summary statistics of the six particle tracks through each of the seven conceptual models (ℓ is the average path length in meters and *v* is the average velocity in meters per year). The values in parentheses are the standard deviations.

Conceptual Model	Particle 1	Particle 2	Particle 3	Particle 4	Particle 5	Particle 6
CH ℓ (m)	571 (42)	1423 (135)	1043 (191)	2348 (196)	1723 (428)	1585 (177)
CH *v* (m/yr)	5.044 (2.138)	1.979 (1.271)	0.060 (0.0288)	0.066 (0.02)	0.046 (0.084)	0.059 (0.027)
CL ℓ (m)	615 (255)	1371 (381)	1428 (208)	1942 (110)	2468 (448)	2121 (170)
CL *v* (m/yr)	0.265 (0.283)	0.190 (0.111)	0.048 (0.018)	0.028 (0.01)	0.053 (0.017)	0.055 (0.012)
WH ℓ (m)	713 (90)	2214 (170)	962 (58)	2498 (456)	1948 (407)	1791 (179)
WH *v* (m/yr)	0.268 (0.122)	0.166 (0.056)	0.080 (0.027)	0.109 (0.031)	0.056 (0.02)	0.086 (0.02)
WL ℓ (m)	728 (98)	2181 (318)	956 (52)	2759 (287)	1920 (430)	1781 (143)
WL *v* (m/yr)	0.271 (0.128)	0.170 (0.062)	0.084 (0.03)	0.100 (0.020)	0.063 (0.126)	0.075 (0.019)
EH ℓ (m)	714 (91)	2260 (180)	1007 (100)	2909 (357)	1746 (260)	1513 (43)
EH *v* (m/yr)	0.278 (0.132)	0.164 (0.054)	0.066 (0.03)	0.093 (0.027)	0.064 (0.015)	0.081 (0.026)
EL ℓ (m)	732 (94)	2232 (318)	1028 (125)	2707 (125)	1760 (268)	1534 (45)
EL *v* (m/yr)	0.266 (0.122)	0.169 (0.063)	0.062 (0.029)	0.098 (0.022)	0.066 (0.017)	0.081 (0.026)
NF ℓ (m)	733 (94)	2236 (334)	1037 (188)	2755 (429)	1749 (252)	1498 (171)
NF *v* (m/yr)	0.266 (0.121)	0.168 (0.062)	0.061 (0.029)	0.099 (0.022)	0.067 (0.017)	0.083 (0.042)

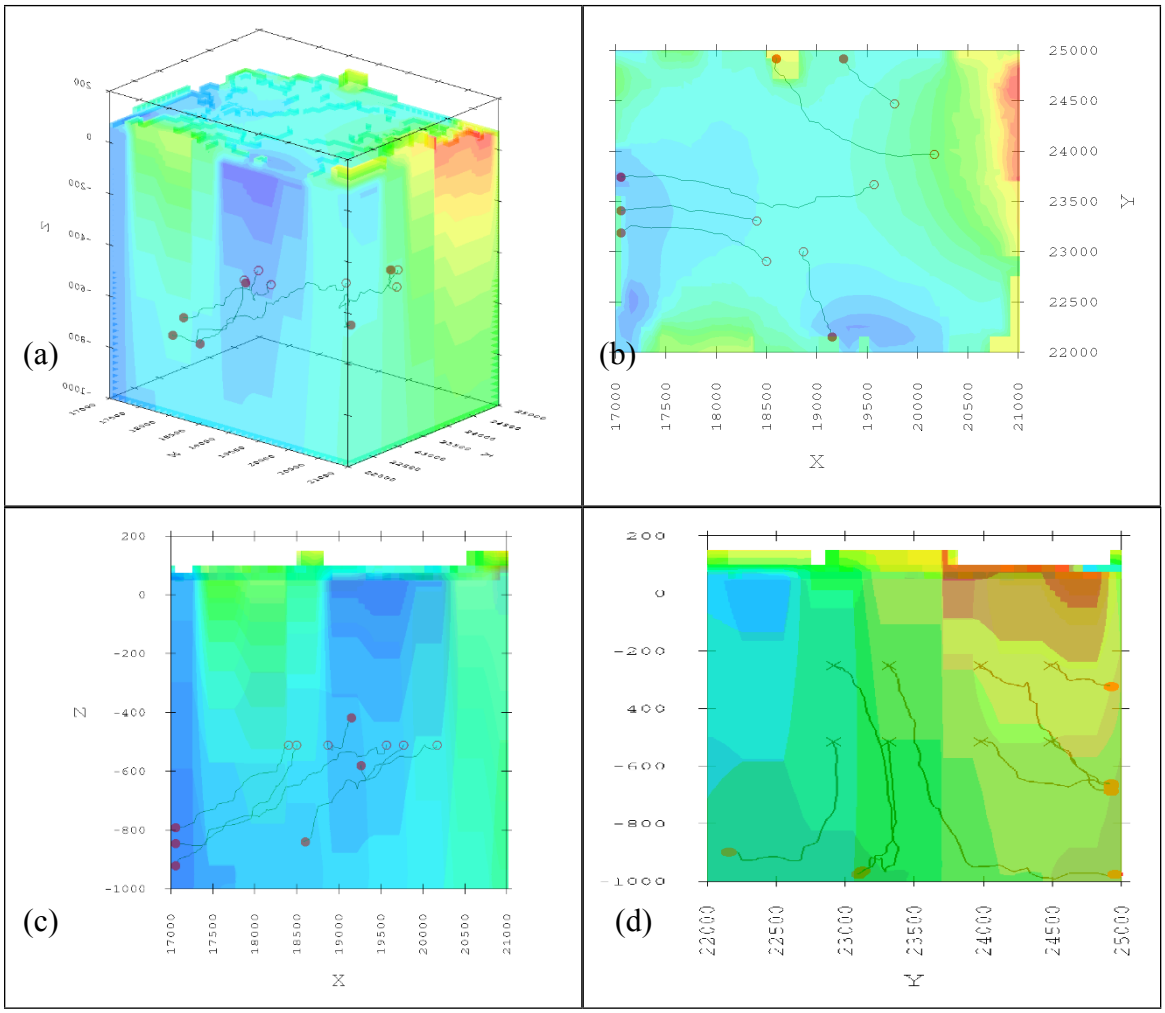

Figure 4: Particle tracks for the flow field corresponding to Figure 3c (centered low hydraulic conductivity fault, Case CL) for the (a) oblique view, (b) top (*x*-*y*) view, (c) side (*x*-*z*) view, and (d) front (*y*-*z*) view.

Plan views of the 50 (x, y) particle tracks for each conceptual model with the low hydraulic conductivity Oomagari fault for particles released 500 m down each borehole (Particles 1–6 correspond to HDB-1, -3, -4, -5, -6, and -8, respectively) are shown in Figure 5 (Cases CL, WL, EL, and NF). Figure 6 shows the particle tracks for the same particles, but this time with the Oomagari fault modeled as a high hydraulic conductivity feature (Cases CH, WH, EH, and NF). The thick red line indicates the location of the top of the Oomagari Fault. Note that the particle tracks for conceptual models with the fault in the east (Cases EL and EH) and with no fault (NF) are similar because in the east fault cases, the fault is far enough away from the particle tracks to have no significant impact on their paths. As noted above, differences between individual pathways in the same conceptual model are due to variations in the random stochastic material field yielding local differences in the flow field. In comparing across fault location conceptual models and across fault conductivities in Figure 4 and 5, it is clear that both the location and conductivity of the fault may significantly impact particle paths. Clearly, the exact location of the fault as well as its hydraulic conductivity is critical to determining flowpaths. In comparing Figure 5 and Figure 6, it is apparent that the flow field changes noticeably between the conceptual models for Cases CL and CH while others have fewer differences. Note that in Figure 5 and Figure 6 the particle tracks shown in Case NF are, of course, identical. It is perhaps surprising that in Figure 6 the fault does not act as a conduit to flow. In fact, due to the boundary conditions, the flow where Particle 2 intersects the fault is almost exactly westward and thus the particle traverses the fault entirely before exiting. Note that the flowpaths of Particles 2 and 4 are more northerly in Case CH than CW in accord with the fault orienting the entire flow field in its direction.

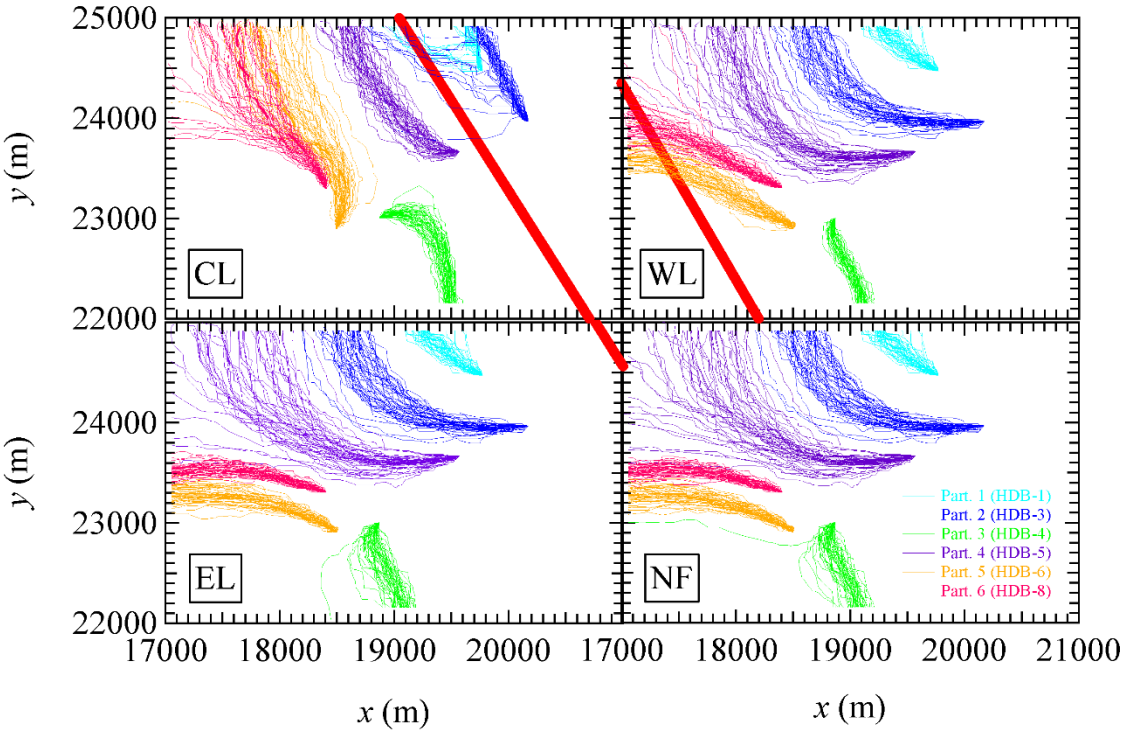

Figure 5: Particle tracks for the fifty realizations of each conceptual model (particles released 500 m down each borehole). The thick red line indicates the location of the top of the low hydraulic conductivity Oomagari Fault.

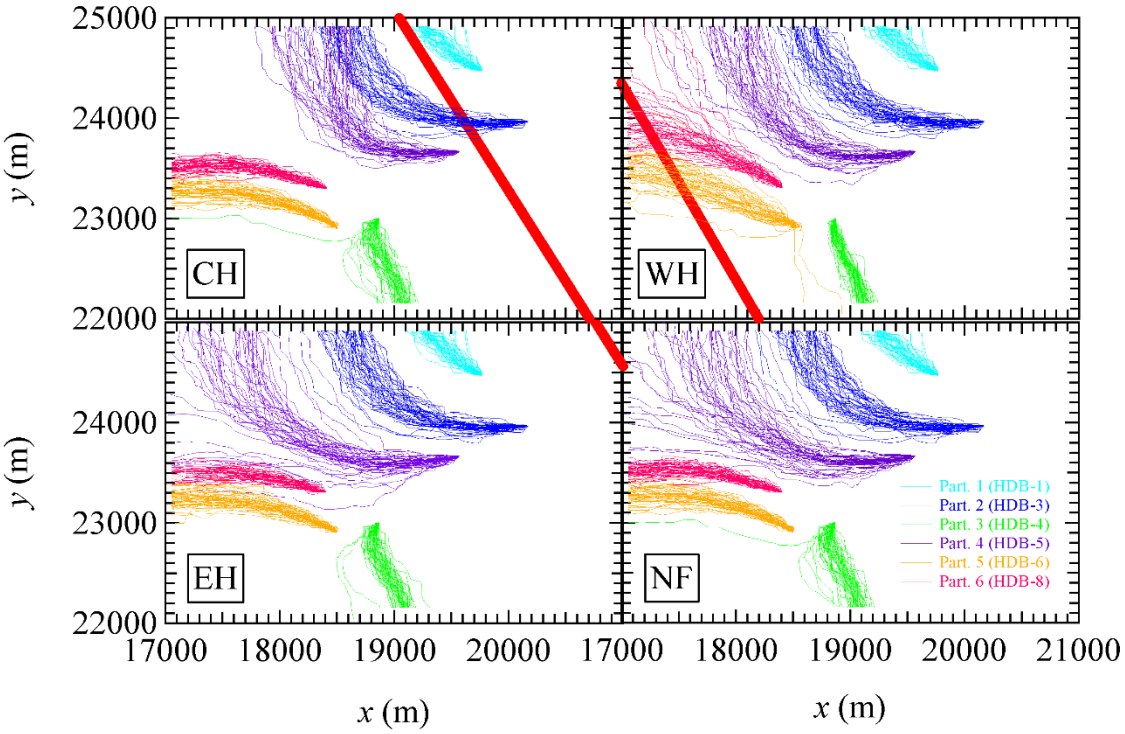

Figure 6: Particle tracks for the fifty realizations of each conceptual model (particles released 500 m down each borehole). The thick red line indicates the location of the top of the high hydraulic conductivity Oomagari Fault.

The mean path length and velocities for each particle are listed in Table 3 and shown graphically in Figure 7. Primary differences lie in the models where the Oomagari Fault is centered (Cases CL and CH). For example, Particles 1 and 2 in the centered high hydraulic conductivity fault model (Case CH) have velocities more than an order of magnitude greater than other conceptual models because they travel through this conductive feature. In addition, for Case CL, particle path lengths can either be longer (Particles 3, 5, and 6) or shorter (Particle 4) depending upon the release point and the velocity field resulting from the high or low hydraulic conductivity fault.

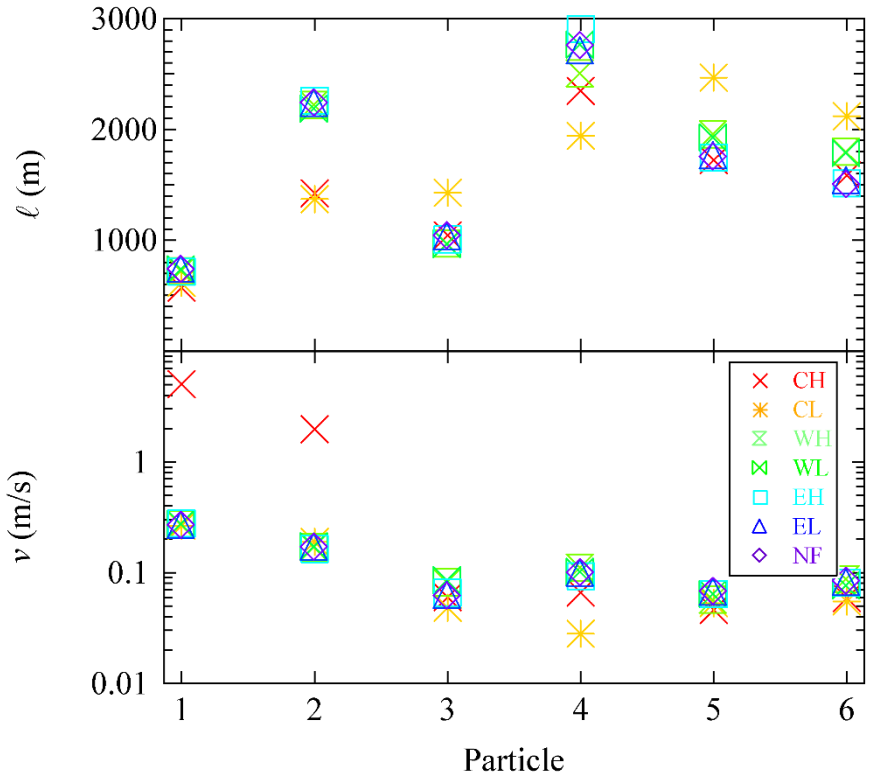

Figure 7: Average path length and velocity for the six particles released from each of the seven conceptual models.

3.2 The F-Ratio

Conceptually, the F-ratio can be thought of as the ratio of factors resisting transport (i.e., path length and surface area available for diffusion) to those factors driving transport (i.e. velocity). The F-ratio is defined as (SKI, 1997)

$$F = \frac{\mathrm{l} \times S_A}{v_D} = \frac{t \times S_A}{\theta}, \qquad \text{* MERGEFORMAT (7)}$$

where ℓ is the MODPATH path length through a model cell, S_A is the surface area of fractures in a grid block, v_D is the Darcy velocity in a model cell, t is the travel time through a model cell, and θ is the porosity of the model cell. Thus, there is a value of F calculated for each model cell through which a particle travels. The F-ratio calculations require assumptions about the fracture frequency and the amount of the fracture surface that is actually in contact with zones of significant advection. The S_A for each model cell depends upon the material type as specified by the material fields generated by T-PROGS as listed in Table 1 (each fracture is composed of two parallel plates separated by the fracture aperture). Note that there is always three times the number of fractures per block listed in Table 4 to account for all three orthogonal directions and that the number of fractures per meter is the median of the values listed in Table 1 for that material. Although each material could be assigned a unique porosity, F would remain unchanged because the travel time, t, as calculated from MODPATH, is inversely proportional to the porosity. The entire model domain is assigned a porosity of 0.3, which is consistent with the Quintessa model and previous models of the URL. For the

calculation of F, the proportion of the fracture surface in contact with actively flowing water is assumed to be 5 percent (McKenna et al., 2001).

Table 4: Fracture frequency and corresponding surface area for each material type.

Material	Fractures/m	Fractures/m^3	S_A (m^2)
1	0.5	1.5	3
2	3	9	18
3	8	24	48
4	13	39	78
5	18	54	108

Box and whisker plots were generated to examine the statistics of F for each particle. For all box and whisker plots, the blue lines are the median values, the yellow boxes indicate the ranges for the 25th to 75th percentiles, the green whiskers indicate the 5th and 95th percentiles, and the red circles are outliers that reside beyond the 95th percentiles. These (few) high values are caused by long residence times in a model cell with a low hydraulic gradient and/or low hydraulic conductivity, which is inherently a rare occurrence because flowpaths tend to avoid these cells. It was shown previously that F increases with material type (James, 2004) and the same is true for these simulations because S_A (i.e. fracture frequency) increases with material type. Across different particles, no simple relationship exists between their F-ratio. However, it is important to note the similarities between cases with an east fault (Cases EL and EH) and that with no fault (Case NF) in both figures. This is expected because when the fault is located in the east of the model domain, there is minimal impact on the particle tracks because the conceptual model is nearly equivalent to the case with no fault (see Figure 5 and Figure 6 for evidence of similar particle paths). Note that the low median values for Particles 1 and 2 of Case CH correspond to the high velocities noted in Figure 7. When the centered fault acts as a high hydraulic conductivity feature, the F-ratio decreases because particles are more quickly advected toward the model boundaries.

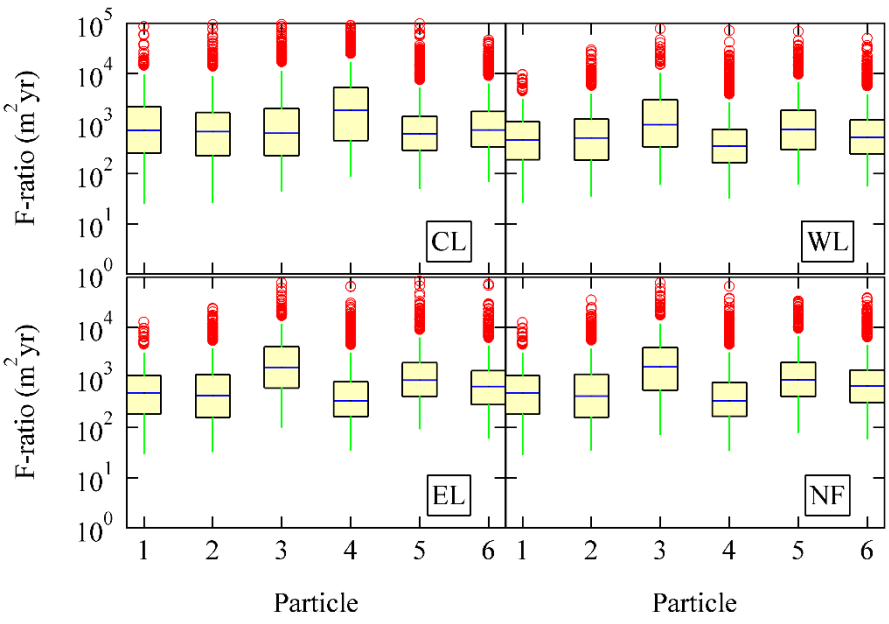

Figure 8: F-ratio distribution for each particle when the Oomagari fault is a low hydraulic conductivity feature (Cases CL, WL, EL, and NF).

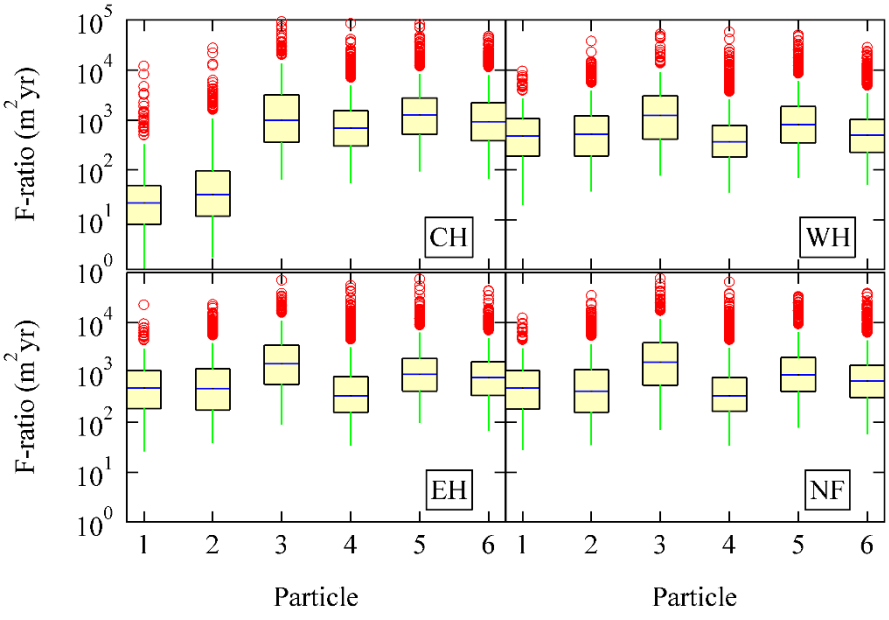

Figure 9: F-ratio distribution for each particle when the Oomagari fault is a high hydraulic conductivity feature (Cases CH, WH, EH, and NF).

Clearly, the conceptual model of fault hydraulic conductivity impacts the F-ratio with high hydraulic conductivity faults tending to decrease the calculated *F* values as expected. This is apparent in the increased number of outliers (red circles) in Cases CL and WL compared to Cases CH and WH.

In addition to F being calculated for each model cell through which a particle passes, the time weighted F-ratio was also calculated for each of the fifty realizations (particle tracks) of the seven conceptual models. Time weighting of the F-ratio is calculated as

$$F_{\text{weighted}} = \sum_{i=1}^{n} \frac{t_i}{t_{\text{total}}} F, \qquad \text{* MERGEFORMAT (8)}$$

where t_i is the time spent in cell i and t_{total} is the total travel time in the model domain through n cells. Box and whisker plots for each of the particles in each conceptual model are shown in Figure 10 and Figure 11. As before, there is a strong similarity between Cases EH, EL, and NF. Overall, the high values for F indicate a potential for significant retardation (a great deal of diffusion and small velocities). Time-weighted median F-ratios tend to be higher than the median F-ratios for each cell because the averaging process weighs longer residence times more heavily and longer residence times correspond to higher F-ratios (notice that the minimum value of the F-ratio is 10^2 m^2/yr in Figure 10 and Figure 11 and 10^0 m^2/yr in Figure 8 and Figure 9). Note also that in comparison to the range of F-ratios calculated across model cells (Figure 8 and Figure 9), that time weighted F-ratios span a much smaller range because high and low model cell values are damped through the averaging process. There are also fewer outliers. The hydraulic conductivity of the fault has a notable impact on the weighted F-ratio distribution for some particles. Particles 1 and 2 show much lower weighted F-ratios for case CH because they often enter the high hydraulic conductivity zone and are transported more quickly to the model boundary. In general, distributions for conceptual model Cases CL and CH (where fault conductivity significantly impacts particle paths) are wider than for Cases WL, WH, EL, EH, and NF where the fault has a smaller impact on particle paths.

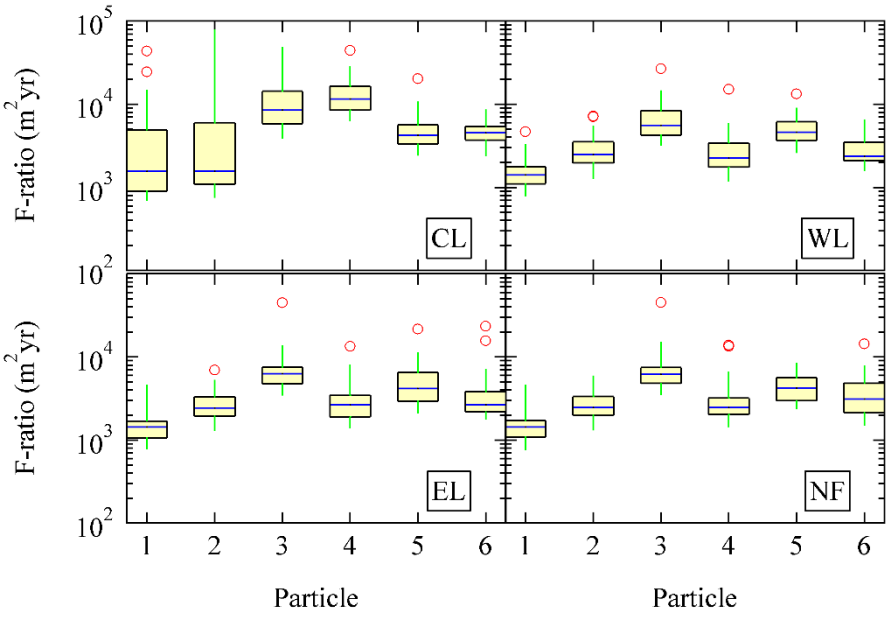

Figure 10: Box and whisker plots of the time weighted F-ratio for each particle and each conceptual model with the Oomagari fault as a low hydraulic conductivity feature (Cases CL, WL, EL, and NF).

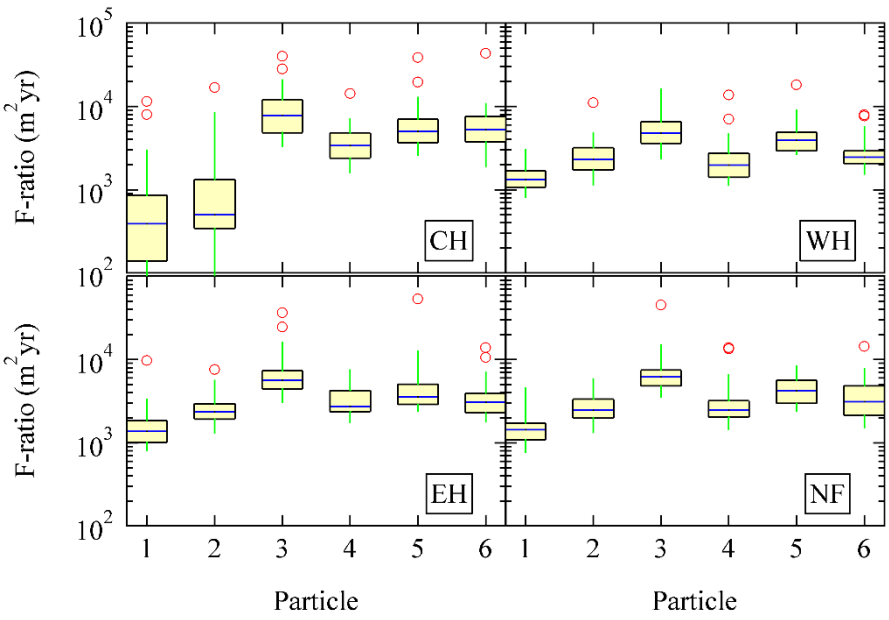

Figure 11: Box and whisker plots of the time weighted F-ratio for each particle and each conceptual model with the Oomagari fault as a high hydraulic conductivity feature (Cases CH, WH, EH, and NF).

4. Solute Transport

In the case of the Quintessa model, it is desirable to characterize the fate and transport of solutes through the Horonobe URL. Solute transport is subject to the effects of advection, dispersion, and reaction (e.g., retardation). Clearly, it is advantageous (more accurate) to model all important transport mechanisms over the entire heterogeneous, three-dimensional model domain. However, the computational cost associated with such a comprehensive model is prohibitive. Thus, a simpler model abstraction was used to predict fate and transport of a solute.

As described above, GMS was used to solve the flow field of the heterogeneous hydraulic conductivity field and MODPATH was then used to simulate the transport of particles in the flow field due solely to advection. All 6 particles' starting locations at 500 m down each borehole were modeled for each of the 50 realizations yielding 300 particle tracks for each conceptual model of the fault. Assuming that the solute follows a particle path, an analytical transport solution can be used to predict contaminant concentrations along the path over time assuming that dispersion across streamlines does not affect the particle's path. This technique provides a one-dimensional approximation of transport. This transport abstraction may be solved with the one-dimensional advection-dispersion-reaction transport equation,

$$R_{eff}\frac{\partial C(x,t)}{\partial t}=D_{eff}\frac{\partial^2 C(x,t)}{\partial x^2}-U_{eff}\frac{\partial C(x,t)}{\partial x}, \quad \text{* MERGEFORMAT (9)}$$

where R_{eff} is the effective retardation constant, D_{eff} is the effective dispersion coefficient, U_{eff} is the effective or average velocity, C is the solute concentration, x is the distance along the path length, and t is time. For the case of a constant concentration at the source ($x = 0$), the appropriate boundary and initial conditions are:

$$C(0,t)=C_0, \quad \text{* MERGEFORMAT (10)}$$

$$C(\infty,t)=0, \qquad \text{* MERGEFORMAT (11)}$$

$$C(x,0)=0, \qquad \text{* MERGEFORMAT (12)}$$

where C_0 is the concentration of the source. Assuming a value of unity (or normalized concentration) for C_0, the transport equation with the previous boundary and initial conditions has the analytical solution (James and Chrysikopoulos, 2003):

$$C(x,t)=\frac{1}{2}\left\{\operatorname{erfc}\left[\frac{R_{eff}x-U_{eff}t}{2\sqrt{R_{eff}D_{eff}t}}\right]+\exp\left(\frac{xU_{eff}}{D_{eff}}\right)\operatorname{erfc}\left[\frac{R_{eff}x+U_{eff}t}{2\sqrt{R_{eff}D_{eff}t}}\right]\right\}. \text{* MERGEFORMAT (13)}$$

Effective properties are based upon the material properties along the transport paths that can be determined through the particle tracking data (model cells traversed, total path length, and travel time).

A retardation factor for each material type must be assigned. Table 5 lists the assumed retardation factors for each material type showing decreasing retardation with increasing fracture frequency (more retardation through lower hydraulic conductivity model cells). In a real PA analysis, these assumptions would require justification.

Table 5: Material type and corresponding assumed retardation coefficient.

Material	R
1	1.4
2	1.3
3	1.2
4	1.1
5	1

Because the specific cells that are traversed and the corresponding retardation of each material along a particle's path are known, an effective retardation factor may be calculated by length-weighting the retardation factor of each material through which a particle passes:

$$R_{eff}=\frac{\sum_i R_i L_i}{\sum_i L_i}, \qquad \text{* MERGEFORMAT (14)}$$

where R_i and L_i are the local retardation coefficient and path length through cell i, respectively. The total path length from borehole injection to model boundary is used to calculate R_{eff}.

Using the particle tracking data, the effective velocity is calculated by simply dividing the total path length by the total travel time

$$U_{eff}=\frac{L_{total}}{t_{total}}, \qquad \text{* MERGEFORMAT (15)}$$

where L_{total} is the total path length of a particle from its release point to the model boundary.

The effective longitudinal dispersion can be calculated from the dispersivity by the relationship (Fetter, 1992, eq. 2.11a)

$$D_{eff} = U_{eff}\sigma, \qquad \text{* MERGEFORMAT (16)}$$

where σ is the longitudinal dynamic dispersivity. The dispersivity can be estimated from the total length of the particle's path using the empirical relationship derived by Xu and Eckstein (1995)

$$\sigma = 0.83\left[\log_{10}\left(L_{total}\right)\right]^{2.414}. \qquad \text{* MERGEFORMAT (17)}$$

For each solution, R_{eff}, U_{eff}, and D_{eff} specific to each particle path were calculated with * MERGEFORMAT (14), * MERGEFORMAT (15), and * MERGEFORMAT (16), respectively. These values were substituted into * MERGEFORMAT (13) and solute concentration breakthrough curves were calculated for each particle path at $x = L_{total}$. A total of 50 breakthrough curves for each particle in each of the seven conceptual models were generated. Breakthrough curves for each particle and each conceptual model were combined to yield an ensemble average breakthrough curve of concentration as a function of time across all 50 hydraulic conductivity field realizations.

Figure 12 shows the ensemble-averaged breakthrough curves for each particle and each conceptual model. The breakthrough curves show that it can take less than 100,000 yrs for the solute to reach the boundary and it typically takes 1,000,000 yrs for the constant source to saturate the boundary of the model. Note that retardation has a major impact on breakthrough because unretarded travel times range from on the order of 100 to 100,000 yrs. Such long breakthrough times are a function of the model boundary conditions and the correspondingly slow flow field and should be re-examined in an actual PA model. Most of the breakthrough curves are similar (Particles 3–6), indicating that these particles are not significantly impacted by the fault location or its hydraulic conductivity (conceptual model). However, there are some notable differences for Particles 1 and 2; Case CH yielded faster transport times than the other fault scenarios for these particles. Recall that for Particles 1 and 2, Case CH exhibited higher average velocities and shorter total pathlengths relative to the other conceptual models. The primary differences seen in the breakthrough curves between the different hydraulic conductivity fields (high or low) for each fault scenario depend on whether the particle paths traverse the fault location because the conceptual model for hydraulic conductivity only changes the fault's characteristics (it impedes or conducts flow). For particle paths that do not encounter the fault, there is little difference in breakthrough curves between the high and low conductivity conceptual models.

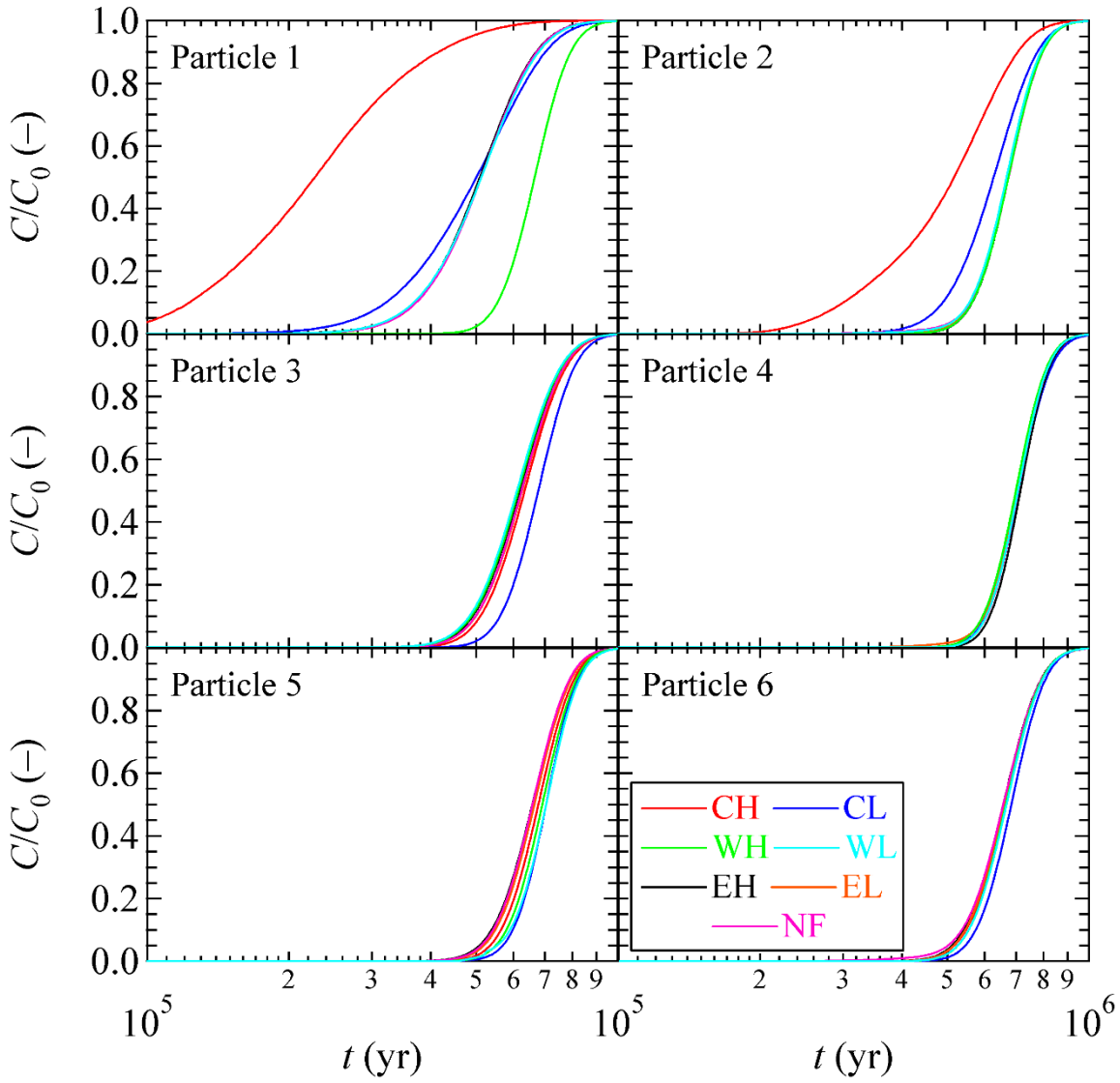

Figure 12: Breakthrough curves for each particle and for each conceptual model.

Figure 13 facilitates a comparison of the breakthrough curves for Cases CL, CH, WL, and WH. Note that particularly for these conceptual models, both the location of the fault and its hydraulic conductivity are important when estimating solute transport. Thus, establishing the fault location and determining its characteristics are critical for PA modeling. Although all the breakthrough curves for each fault scenario are similar in Figure 13, the results are shown on a log time scale disguise what are reasonably large differences in breakthrough time.

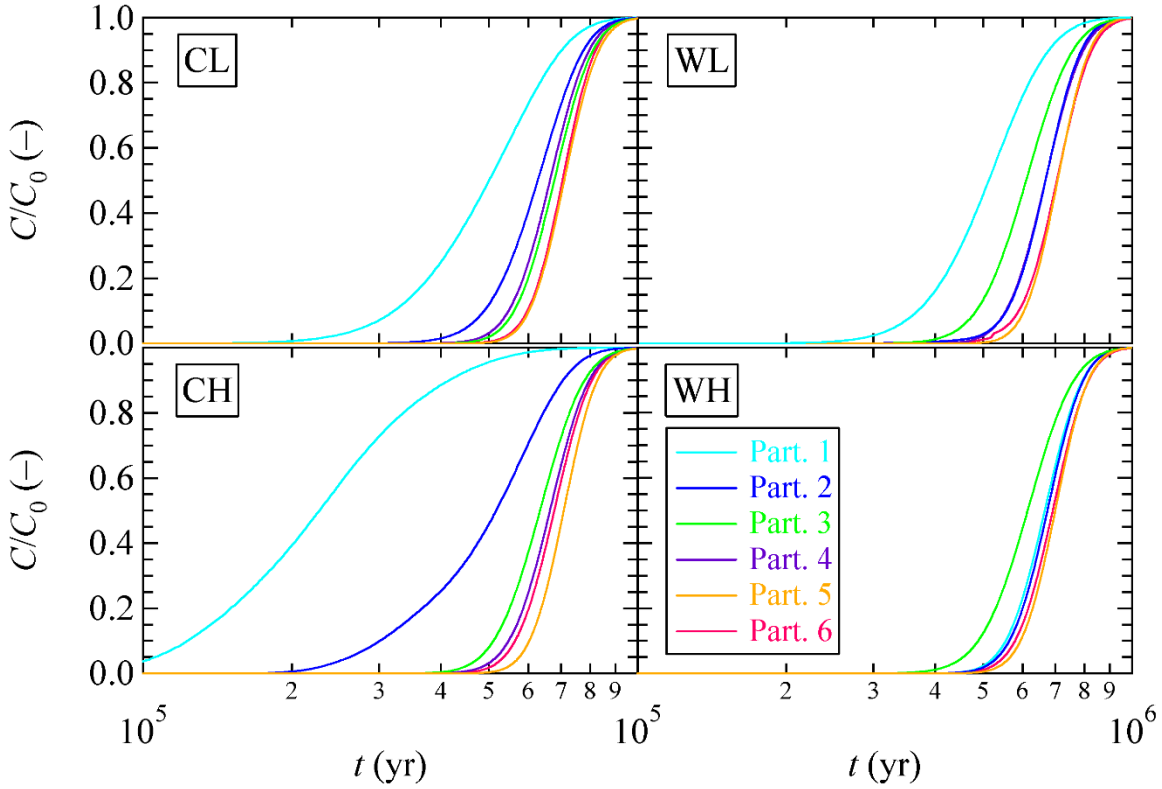

Figure 13: Comparison of breakthrough curves for Cases CL, CH, WL, and WH for each particle.

5. Discussion and Conclusions

Individual path lengths and velocities for each particle and each realization are presented in Table 3. Several conclusions may be inferred from these results. For example, on average, Particles 1 and 2 are significantly impacted when the Oomagari Fault is near the center of the model (Cases CL and CH). Other conceptual models (non-centered faults, Cases WL, WH, EL, EH, and NF) do not significantly impact particle path lengths and velocities. This indicates that the location and characteristics of the fault are critical to PA modeling, especially if the fault is near the center of the model.

The F-ratio as a measure of retarding (diffusion across surface area) to advancing forces (velocity) indicates that significant retardation should be expected from both sorbing and non-sorbing radionuclides, due to high values of F. It should be noted, however, that the presence of colloids could negate much of the diffusive retarding forces. That is, colloids could act as a mobile third phase that may carry radionuclides significantly farther and faster than expected (Kersting et al., 1999). For Case CH, particles released close to the fault (Particles 1 and 2) show significantly lower F-ratios. This is because the high hydraulic conductivity fault acts as a conduit to flow and can result in increased velocities. Again, the location and characteristics of the fault are important factors in assessing how well the site is expected to perform as a repository.

A one-dimensional transport abstraction also indicates that solute breakthrough curves are subject to the location and characteristics of the Oomagari Fault. This is most evident for particles whose paths intersect the fault. Particles 1 and 2 are particularly impacted, especially

when they traverse the fault for Case CH because they are quickly transported to the model boundary. Comparison to a more detailed three-dimensional model is warranted once the necessary computational resources become available.

Overall, this modeling effort indicates that a more thorough identification of the fault location and properties would most significantly reduce the uncertainty in this PA model. Therefore, it is recommended that a thorough characterization of the Oomagari Fault be undertaken. In addition, it is important to identify primary material types expected within the model domain and to correlate parameters such as fracture frequency with hydraulic conductivity, surface area, and retardation factor.

One irregularity that must be addressed is that the modeled flow field is generally downward (-*z* direction) while at the Horonobe URL the flow field is typically upward (+*z* direction). This is due to the boundary conditions supplied by Quintessa from their regional-scale model. Because their model was intended to reproduce the conditions expected during dewatering of the site, the steady-state direction of the flow field is of little importance to that application. For PA modeling, however, it is critical to accurately represent steady-state conditions and, in practice, this model should be revised (possibly with a different recharge boundary condition) to yield the expected upward flow field.

5. References

Carle, S. F., *T-PROGS: Transition Probability Geostatistical Software Version 2.1*, Hydrologic Sciences Graduate Group, University of California, Davis, 1999.

EMRL, *GMS 5.0 Tutorial*, Environmental Modeling Research Laboratory, Brigham Young University, 2003.

Fetter, C. W., *Contaminant Hydrogeology*, Prentice Hall, Upper Saddle River, New Jersey, 1992.

James, S.C., *An Example Uncertainty and Sensitivity Analysis at the Horonobe Site for Performance Assessment Calculations*, SAND2005-517451743440, Albuquerque, NM, 28 p., 2004.

James, S. C. and C. V. Chrysikopoulos, Analytical solutions for monodisperse and polydisperse colloid transport in uniform fractures, *Colloids Surf. A. Physicochem. Eng. Aspects*, 226, 101–118, 2003.

Kersting, A. B., D. W. Efurd, D. L. Finnegan, D. J. Rokop, D. K. Smith, and J. L. Thompson, Migration of plutonium in groundwater at the Nevada Test Site, *Nature*, 397, 56–59, 1999.

McKenna, S. A., M. Eliassi, K. Inaba, and H. Saegusa, Steady-state groundwater flow modeling of the MIU Site area, SAND2005-517451743570C, Sandia National Laboratories, Albuquerque, NM, 14p., 2001.

SKI, SKI Site-94 Deep repository performance assessment project, Swedish Nuclear Power Inspectorate, SKI Report 97:5, Stockholm, Sweden, 1997.

Xu, M. J. and Y. Eckstein, Use of weighted least-squares method in evaluation of the relationship between dispersivity and field-scale, *Ground Water*, **33**(*6*), 905–908, 1995.

Distribution

FOREIGN DISTRIBUTION:

Takanori Kunimaru
Miyazono-machi 1-8, Horonobe-cho,
Hokkaido, Japan 098-3207

Hiroshi Kurikami
Miyazono-machi 1-8, Horonobe-cho
Hokkaido, Japan 098-3207

Hitoshi Makino (5)
4-33, Muramatsu, Tokai-Mura, Naka-Gun
Ibaraki, Japan 319-1194

Seiichiro Mitsui
4-33, Muramatsu, Tokai-Mura, Naka-Gun
Ibaraki, Japan 319-1194

Keiichiro Wakasugi (2)
4-33, Muramatsu, Tokai-Mura, Naka-Gun
Ibaraki, Japan 319-1194

Shinichi Yamasaki (2)
Miyazono-machi 1-8, Horonobe-cho
Hokkaido, Japan 098-3207

Mikazu Yui
4-33, Muramatsu, Tokai-Mura, Naka-Gun
Ibaraki, Japan 319-1194

SANDIA INTERNAL:

1	MS 0735	6115	S. J. Altman
1	MS 0735	6115	R. E. Finley
4	MS 0735	6115	S. C. James
1	MS 0735	6115	T. S. Lowry
1	MS 0735	6115	S. A. McKenna
1	MS 0735	6115	M. D. Reno
1	MS 0751	6117	R. P. Jensen
1	MS 0778	6852	B. W. Arnold
2	MS 0899	9616	Technical Library
1	MS 9018	8945-1	Central Technical Files
1	MS 1393	12100	E. K. Webb